ACS Energy LETTERS

http://pubs.acs.org/journal/aelccp

LETTER

Compositional Tuning of Carrier Dynamics in $Cs_2Na_{1-x}Ag_xBiCl_6$ Double-Perovskite Nanocrystals

Dongxu Zhu,[▽] Juliette Zito,[▽] Valerio Pinchetti,[▽] Zhiya Dang, Andrea Olivati, Lea Pasquale, Aiwei Tang, Matteo L. Zaffalon, Francesco Meinardi, Ivan Infante,* Luca De Trizio,* Liberato Manna,* and Sergio Brovelli*

Cite This: *ACS Energy Lett.* 2020, 5, 1840−1847

Read Online

ACCESS | Metrics & More | Article Recommendations | Supporting Information

ABSTRACT: We devised a hot-injection synthesis to prepare colloidal double-perovskite $Cs_2NaBiCl_6$ nanocrystals (NCs). We also examined the effects of replacing Na^+ with Ag^+ cations by preparing and characterizing $Cs_2Na_{1-x}Ag_xBiCl_6$ alloy NCs with x ranging from 0 to 1. Whereas $Cs_2NaBiCl_6$ NCs were not emissive, $Cs_2Na_{1-x}Ag_xBiCl_6$ NCs featured a broad photoluminescence band at ∼690 nm, Stokes-shifted from the respective absorption by ≥1.5 eV. The emission efficiency was maximized for low Ag^+ amounts, reaching ∼3% for the $Cs_2Na_{0.95}Ag_{0.05}BiCl_6$ composition. Density functional theory calculations coupled with spectroscopic investigations revealed that $Cs_2Na_{1-x}Ag_xBiCl_6$ NCs are characterized by a complex photophysics stemming from the interplay of (i) radiative recombination via trapped excitons localized in spatially connected $AgCl_6$−$BiCl_6$ octahedra; (ii) surface traps, located on undercoordinated surface Bi centers, behaving as phonon-assisted nonradiative decay channels; and (iii) a thermal equilibrium between trapping and detrapping processes. These results offer insights into developing double-perovskite NCs with enhanced optoelectronic efficiency.

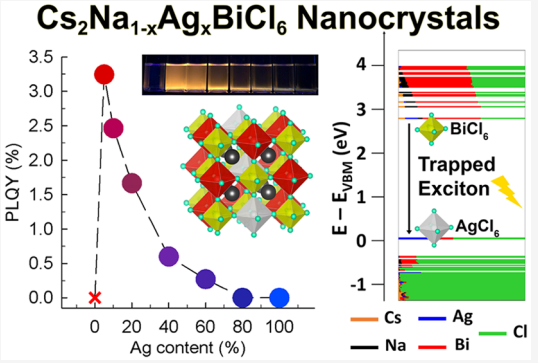

Nanocrystals (NCs) of lead halide perovskites have attracted significant interest in recent years and are promising candidate materials for various optoelectronic applications.[1−7] However, given the intrinsic toxicity of lead, which constrains the use of such materials in commercial devices, the scientific community is now seeking for alternative stable lead-free metal halide perovskite compounds with comparable optical properties.[8,9] The most promising candidates in this context are the so-called double perovskites (DPs), also termed *elpasolites*, having the general formula $A_2B^+B^{3+}X_6$, characterized by a 3D perovskite structure made of alternating $[B^+X_6]$ and $[B^{3+}X_6]$ corner-sharing octahedra with A^+ ions occupying the voids in between.[8−11] The different combinations of possible A^+, B^+, and B^{3+} ions create a richness of structures, making the *elpasolites* family particularly interesting from a chemistry and a materials science point of view,[10] as well as for technological applications in photovoltaics,[12−14] artificial lighting, and photon management.[15]

In the last couple of years, various DP materials featuring interesting optical properties have been synthesized at the nanoscale, comprising Cs_2AgBiX_6 (X = Cl, Br, I), $Cs_2AgInCl_6$, $Cs_2NaInCl_6$, $Cs_2NaBiCl_6$, and Cs_2AgSbX_6 NCs (X = Cl, Br).[16−29] Unluckily, all these systems feature a weak PL emission because they have either an indirect band gap (Cs_2AgBiX_6, Cs_2AgSbX_6) or a direct band gap characterized by a parity-forbidden transition ($Cs_2AgInCl_6$) or by a parity-allowed transition albeit with a weak oscillator strength (Cs_2NaInX_6 and Cs_2NaBiX_6).[9−11,24,30−32] As a result, the interplay between radiative and nonradiative processes makes the excitonic photophysics of these materials significantly more complex than for the case of lead halide perovskites. This calls for specific multidisciplinary investigations to trace rational guidelines for their optimization. In turn, the control and the design of highly performing DP materials has great technological implications, as it will enable us to reap the benefits of their intrinsically broad and largely Stokes-shifted

Received: April 28, 2020
Accepted: May 8, 2020
Published: May 8, 2020

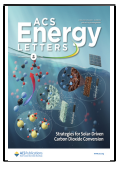

luminescence that makes them particularly appealing for heavy-metal-free, single-component white light-emitting diodes[15] and for transparent luminescent solar concentrators for building-integrated PV applications.[33]

In order to enhance the photoluminescence (PL) of these compounds, different strategies have been already pursued which involved doping, alloying, or both. Doping $Cs_2AgInCl_6$ NCs with either Mn^{2+} or Bi^{3+} ions was observed to yield an orange emission with PL efficiency (Φ_{PL}) of ∼16% and 11%, respectively.[18,23] Different groups reported the doping of $Cs_2AgInCl_6$ NCs with rare earth (RE) ions, which led to a near-infrared (NIR) emission at ∼1000 nm with Yb^{3+} and ∼1537 nm with Er^{3+}.[19,34] Chen et al. further extended Yb^{3+} and Mn^{2+} doping to Cs_2AgBiX_6 (X = Cl, Br) NCs.[17] On the other hand, alloying strategies, mainly involving Bi^{3+}, In^{3+}, and Sb^{3+} as B^{3+} cations and Ag^+ and Na^+ as B^+ cations, were exploited to induce an indirect-to-direct band gap transition in DPs with a consequent increase of their PL quantum yield.[21,26,29,31,35−38]

For example, Luo et al. showed that simultaneous doping and alloying can boost the emission of $Cs_2AgInCl_6$: the use of a minimal amount of Bi^{3+} dopants (1%) together with Na^+ cations resulted in Bi-doped $Cs_2Ag_{1-x}Na_xInCl_6$ powders with a Φ_{PL} as high as 86% for x = 0.4.[15] Similarly, our group prepared Bi-doped $Cs_2Ag_{1-x}Na_xInCl_6$NCs with a bright and broad yellow emission which was maximum for x = 0.6 (Φ_{PL} = 22%).[16] Our density functional theory (DFT) calculations revealed that the presence of both Bi^{3+} and Ag^+ cations was essential to optimize the emission of the "host" $Cs_2NaInCl_6$ NCs: the introduction of Bi^{3+} dopants and the substitution of a low percentage of Na^+ with Ag^+ ions led to the formation of a localized $BiCl_6 \rightarrow AgCl_6$ transition. Note that, differently from the common way of describing these materials, we consider the system with Na^+ cations as the reference case, because it presents a wide band gap, with the Na^+ ions acting as electronic barriers (*vide infra*).

Motivated by such results, and inspired by the recent paper by Lamba et al.,[30] we decided to systematically investigate the effects of replacing Na^+ with Ag^+ ions inside $Cs_2NaBiCl_6$ NCs. When the Na/Ag precursor ratio was tuned, a series of $Cs_2Na_{1-x}Ag_xBiCl_6$ NCs were synthesized with an average size around 10 nm and a good size distribution (Scheme 1). These

Scheme 1. Colloidal Synthesis of $Cs_2Na_{1-x}Ag_xInCl_6$ NCs

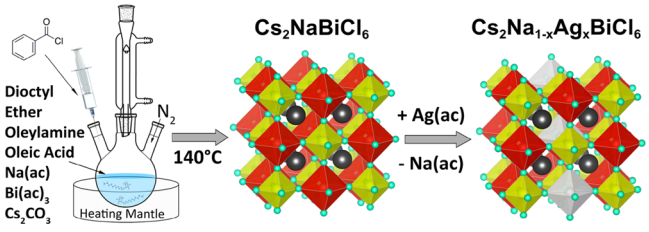

NCs had a broad PL emission around 1.85 eV, which was maximized (∼3% at room temperature) when replacing only a low percentage of Na^+ cations with Ag^+, that is, for the $Cs_2Na_{0.95}Ag_{0.05}BiCl_6$ composition. An in-depth spectroscopic and theoretical investigation of such NC system as a function of the Ag^+ content and temperature revealed a complex photophysics, where the optical efficiency of the NCs results from the interplay between (i) a radiative recombination of trapped excitons (TE) localized in connected $AgCl_6$−$BiCl_6$ octahedra, (ii) their phonon-assisted nonradiative decay, and (iii) a thermal equilibrium between trapping and detrapping of electrons in an intragap defect. This defect is likely associated with surface traps located on undercoordinated Bi centers, whose energy depends on the Na^+ content that ultimately determines the fraction of emissive NCs in the ensemble. Altogether, these processes result in a markedly different temperature dependence of the optical properties of $Cs_2Na_{1-x}Ag_xBiCl_6$ NCs at various Ag^+ content values, whose proper understanding offers useful materials design guidelines to maximize emission efficiency.

$Cs_2Na_{1-x}Ag_xBiCl_6$ NCs were synthesized by a colloidal hot-injection approach in which metal carboxylates and carbonates were reacted with benzoyl chloride to trigger the nucleation and growth of the NCs (Scheme 1). $Cs_2Na_{1-x}Ag_xBiCl_6$ NCs with different compositions (x = 0, 0.05, 0.1, 0.2, 0.4, 0.6, 0.8, 1) were obtained by adjusting the Na/Ag metal precursors ratio, as revealed by both our scanning electron microscope-energy dispersive X-ray spectroscopy (SEM-EDS) and X-ray photoelectron spectroscopy (XPS) analyses (see Experimental Section, Table S1, and Figures S1 and S2 of the Supporting Information).

The X-ray diffraction (XRD) patterns of our NC products showed that they all crystallized in the double-perovskite crystal structure with XRD peaks positioned between those of bulk $Cs_2AgBiCl_6$ (ICSD number 291598) and $Cs_2NaBiCl_6$ (ICSD number 2738), with no presence of secondary phases (Figure 1a). Upon closer inspection, when the Ag^+ content inside the $Cs_2Na_{1-x}Ag_xBiCl_6$ NCs is increased the XRD peaks shifted toward higher 2θ angles, with pure $Cs_2AgBiCl_6$ NCs having lattice parameter of 10.78 Å and pure $Cs_2NaBiCl_6$ NCs of 10.84 Å (Figure 1b). These results indicated the formation of alloyed NCs when working at intermediate Na/Ag compositions. The high-resolution (HR) transmission elecectron microscopy (TEM) characterization of our samples evidenced that the NCs were monocrystalline and exhibited the expected DP structure (Figure 1c−h). The scanning TEM-EDS (STEM-EDS) elemental mapping further supported the formation of alloy NCs in which the different elements were uniformly distributed (Figure 1i).

Theoretical Calculations. To provide a comprehensive picture of the photophysics of $Cs_2Na_{1-x}Ag_xBiCl_6$ NCs, including the effect of both Na^+ and Ag^+ ions, we conducted a multilevel investigation by DFT calculations addressing the main structural and electronic features of these NCs, as well as nonradiative processes associated with structural defects on their surfaces. Initially, we focused on investigating atomistically the mechanism of photoemission, thus paving the way for our spectroscopic measurements of the next section. First, we computed the electronic structure of the cubic $Cs_2NaBiCl_6$ system which, as calculated by Meng et al.,[32] is known to have a direct band gap with a parity-allowed transition. As illustrated in Figure 2a, at the valence band maximum (VBM) the $Cs_2NaBiCl_6$ states are localized on the 3p orbitals of chlorine ions while at the conduction band minimum (CBM) the edge states are mostly localized on the 6p orbitals of Bi ions, as expected. Because of the high ionicity of the bond, the edge-to-edge transition for this system is characterized by a poor spatial overlap, thus accounting for a weak transition dipole matrix element (this is also reported by others on similar systems).[32] As a result, the oscillator strength for this lowest band transition is negligible.

https://dx.doi.org/10.1021/acsenergylett.0c00914
ACS Energy Lett. 2020, 5, 1840−1847

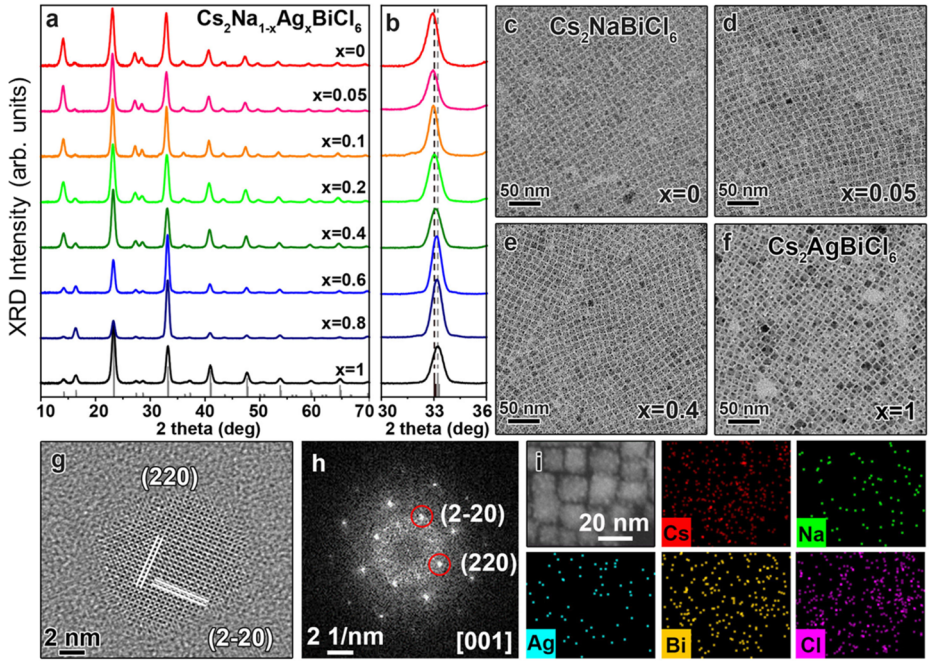

Figure 1. (a) XRD patterns of $Cs_2Na_{1-x}Ag_xBiCl_6$ NCs (x = 0, 0.05, 0.1, 0.2, 0.4, 0.6, 0.8, 1) together with the bulk reflections of $Cs_2AgBiCl_6$ (ICSD number 291598). (b) Magnification of the XRD patterns in the 30°−36° range. The black bars correspond to the bulk $Cs_2AgBiCl_6$ (ICSD number 291598) reflection, while the gray bars correspond to bulk $Cs_2NaBiCl_6$ (ICSD number 2738). (c−f) TEM images of $Cs_2Na_{1-x}Ag_xBiCl_6$ NCs. (g) High-resolution TEM image of a $Cs_2Na_{0.95}Ag_{0.05}BiCl_6$ NC and (h) the corresponding Fast Fourier transform (FFT). (i) STEM-EDS elemental maps of ($Cs_2Na_{0.95}Ag_{0.05}BiCl_6$).

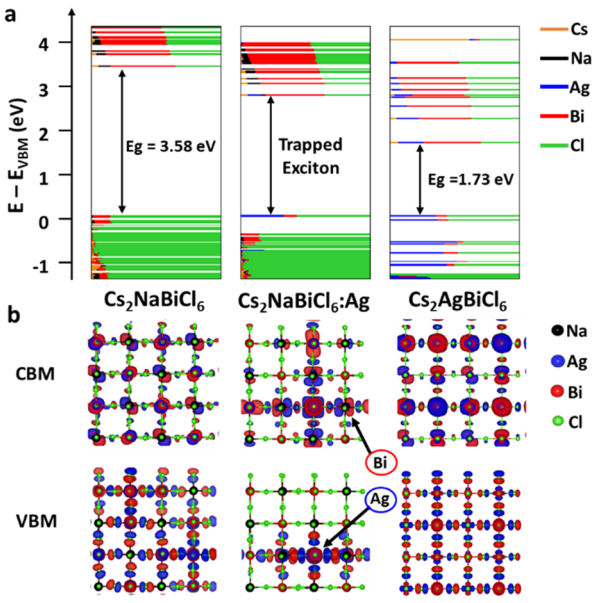

Figure 2. (a) Electronic structure of the $Cs_2NaBiCl_6$, $Cs_2NaBiCl_6$ doped with 1 Ag^+ ion, and $Cs_2AgBiCl_6$ 2 × 2 × 2 supercells computed at the DFT/PBE level of theory on a large 2 × 2 × 2 supercell at the Γ point. Each orbital is represented in real space and decomposed according to each atom type. (b) CBM and VBM orbital plots in real space. The undoped materials present delocalized electron and hole wave functions, while the Ag-doped $Cs_2NaBiCl_6$ system exhibits localization of the wave function.

By introduction of one Ag^+ cation (in substitution of one Na^+) at the center of the $Cs_2NaBiCl_6$ supercell, two main changes were observed in the electronic structure: The first one involved the VB edge, with the formation of two topmost (quasi-degenerated) states composed of a heavily mixed configuration of Ag^+ 4d orbitals ($4d_{z^2}$ and $4d_{z^2-y^2}$, respectively) and Cl^- 3p orbitals that interact in a σ^* antibonding fashion. As illustrated in Figure 2b, the two VB edge states become mainly localized at the $AgCl_6$ octahedron, with only a small contribution of the neighboring $BiCl_6$ octahedra. Such spatial confinement of the hole wave function at the VB edge is ensured by the electropositive Na^+ ions which behave as electronic barriers around the Ag^+ center. Conversely, in pure $Cs_2NaBiCl_6$ the hole wave function is delocalized over the whole supercell. The second important change is the lowering in energy of the CBM state due to the contribution of the 5s orbital of Ag^+. In the stabilized CB edge state, both the Ag^+ 5s orbital and one of the 6p orbitals of the neighboring Bi^{3+} interact in a σ^* antibonding fashion with the directional 3p orbital of the Cl^- ions that connect them spatially. This orbital mixing leads to a partial delocalization of the electron wave function over the six $BiCl_6$ octahedra surrounding the Ag^+ center at the CBM. However, as revealed by the orbital plot in Figure 2b, a further delocalization of the wave function in the supercell is again prevented by the presence of Na^+ ions. Therefore, in a Na-rich $Cs_2Na_{1-x}Ag_xBiCl_6$ system, Ag^+ ions act as centers that are able to localize both holes and electrons at the band edges, thus suggesting the presence of a sizable TE emission, which is compatible with the steady-state and time-resolved PL spectroscopic data shown in the next section.

Because these double-perovskite systems attain only moderate PL efficiency (~3% at room temperature), we can speculate, also because of the experimental evidence presented in the next sections, that nonradiative processes take place at the surface of these NCs. Deep trap states can indeed emerge from an incomplete surface passivation after the synthesis, which leads to the formation of undercoordinated (dangling) ions at the surface.[35,39−41] To probe this effect, we performed

https://dx.doi.org/10.1021/acsenergylett.0c00914
ACS Energy Lett. 2020, 5, 1840−1847

DFT calculations by preparing cubic DP NCs model systems with a $Cs_{324}(Ag+Na)_{108}Bi_{108}Cl_{756}$ stoichiometry. This corresponds to a cube with a side of about 3.0 nm, which is both affordable computationally and relevant from an experimental standpoint (see also Computational Methodology in the Supporting Information for further details). Four different $Cs_2Na_{1-x}Ag_xBiCl_6$ NC models with representative compositions were constructed, featuring x = 0, 0.05, 0.80, and 1, respectively. A survey of their electronic structure is presented in Figure S4. Notably, when their surface was fully passivated, their electronic structures presented either no traps or only shallow ones. On the other hand, when the surface was only partially passivated, then traps began to emerge. To further study this aspect, we analyzed the detachment of surface ions from the outermost surface. This situation was simulated by displacing a neutral CsCl ion pair from one (100) facet in all four NCs models, thus modifying the coordination numbers of some surface atoms. DFT calculations showed that, even after the structural relaxation, a deep trap state localized on a Bi penta-coordinated atom was formed (Figure 3a). The orbital

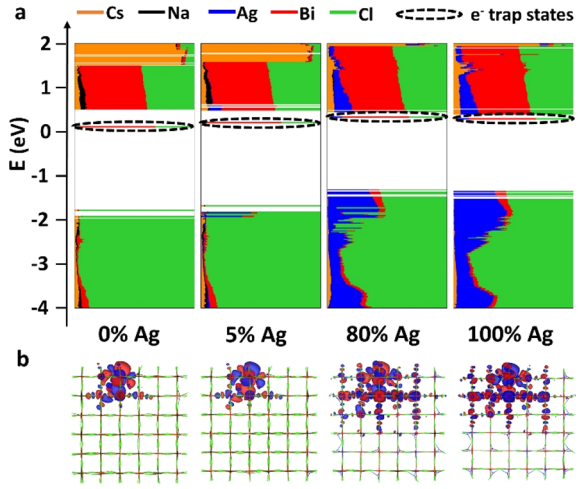

Figure 3. (a) Electronic structures of 3 nm $Cs_2Na_{1-x}Ag_xBiCl_6$ NCs models featuring x = 0, x = 0.05, x = 0.80, and x = 1 after the removal of one CsCl ion pair from the surface. Each line corresponds to a molecular orbital (MO). Each color indicates the contribution of a type of atom for a given MO. The black dotted circles evidence trap states below the CB for all the systems. The position of these electron trap states depends on the Na/Ag ratio of the NC. (b) Lowest unoccupied molecular orbitals (LUMO) plots. The electron wave function localization is more pronounced in the two Na-rich systems (x = 0 and x = 0.05) than in the two Ag-rich ones (x = 0.80 and x = 1).

density plot of this molecular orbital (Figure 3b) shows that for all four NC compositions, such a midgap state appeared and was primarily composed of a single Bi 6p atomic orbital localized on the under-coordinated Bi.

This unoccupied MO within the band gap is therefore likely to behave as an electron trap. In Na-rich NCs, this state is very deep, because the surrounding Na^+ ions confine it on the Bi 6p orbital only. Conversely, in Ag-rich systems the Bi 5c ion can be surrounded by $AgCl_6$ octahedra, which ensure a partial delocalization of the electron wave function. As a consequence, the energetic level associated to the detrimental state is closer to the CB edge and the trap is less deep (i.e., it is shallower). In summary, the presence of Na^+ in $Cs_2Na_{1-x}Ag_xBiCl_6$ DP NCs has the effect of isolating electronically the $BiCl_6$ octahedra. On the one hand, this confinement is essential to obtain a TE that can radiatively recombine at the Ag^+ center. On the other hand, the Na^+ ions increase the degree of localization of the surface trap states, making nonradiative processes more efficient. This result, as it will be shown in the next section, is in line with the temperature- and time-dependent PL measurements varying the Ag^+ content.

Optical Properties of $Cs_2Na_{1-x}Ag_xBiCl_6$ NCs. To investigate the implications of the substitution of Ag^+ for Na^+ cations in our DP NCs experimentally, we performed side-by-side spectroscopic studies as a function of composition and temperature. Upon increasing the fraction of Ag^+ (x) from 0 to 1, the absorption peak linearly shifted from ~3.8 to ~3.3 eV (Figures 4a and S5). At intermediate Ag^+ fractions ($0 < x < 1$),

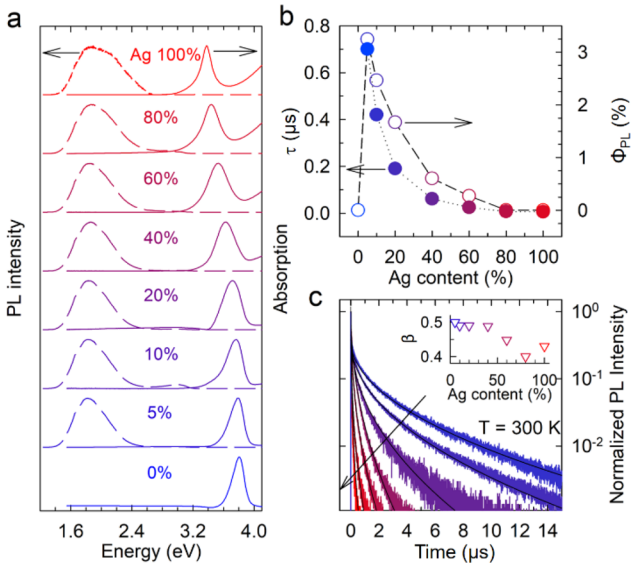

Figure 4. (a) Optical absorption (continuous lines) and PL (dashed lines) spectra of $Cs_2Na_{1-x}Ag_xBiCl_6$ NCs with progressively increasing Ag^+ content (from the blue bottom curve, corresponding to x = 0, to the red top curve, corresponding to x = 1). (b) PL quantum yield, Φ_{PL} (empty circles), and effective lifetime, τ (full circles), extracted by fitting the respective PL decay traces in panel c with stretched exponential functions. The stretching factors, β, are reported in the inset indicating gradually larger disorder with increasing x. All measurements were conducted at room temperature. The color scheme in all panels refers to the code in panel a.

the absorption peak was broader than for the pure compounds ($Cs_2NaInCl_6$ and $Cs_2AgInCl_6$), as also observed in the respective PL excitation (PLE) spectrum reported in Figure S6. All PLE spectra were well reproduced by using a linear combination of the pure $Cs_2NaBiCl_6$ and $Cs_2AgBiCl_6$ excitation peaks, indicating the progressive conversion of pure $Cs_2NaBiCl_6$ into $Cs_2AgBiCl_6$.

Consistent with the negligible oscillator strength computed for $Cs_2NaBiCl_6$,[26] no PL emission was observed from these NCs. In contrast, $Cs_2Na_{1-x}Ag_xBiCl_6$NCs with $x > 0$ featured a broad PL band (fwhm ~550 meV at T = 300 K) with sub-band gap energy of ~1.85 eV (Figures 4a). This, together with the red shift of the absorption peak resulted in the progressive decrease of the Stokes shift (Δ_{SS}) from ~1.9 eV for x = 0.05 to ~1.5 eV for x = 1 (Figure S5). The near invariance of the PL position regardless of the marked change of the band gap energy with varying x is indicative of a recombination

https://dx.doi.org/10.1021/acsenergylett.0c00914
ACS Energy Lett. 2020, 5, 1840−1847

mechanism mediated by TEs, in agreement with the DFT predictions. Upon increasing the Ag^+ content, the PL peak underwent progressive broadening (Figure S5), and the PL efficiency, Φ_{PL}, dropped from over 3% for $x = 0.05$ to below 1% for $x = 1$ (Figure 4b). This is in agreement with the localization effect of Na^+ ions on the electron and hole wave functions evidenced by the DFT study, which reduced inhomogeneous spectral broadening and lowered the probability for nonradiative decay in defect sites. Support to this interpretation was provided by time-resolved PL measurements shown in Figure 4c, where we report the PL decay traces of the $Cs_2Na_{1-x}Ag_xBiCl_6$ NCs. Consistent with a dispersion of TE local configurations inside the NC lattice, all kinetics are well fitted by a stretched exponential function, $I_{PL}(t) = I_0 e^{-(\frac{t}{\tau})^{\beta}}$, with stretching factor β slightly decreasing from 0.5 to 0.4 with increasing x, in agreement with the growing fwhm of the respective PL spectra. With increasing x, the PL dynamics progressively accelerated, with lifetime τ decreasing from ~700 ns for $x = 0.05$ to $\tau \sim 5$ ns for $x = 1$. Importantly, the resulting τ versus x trend resembled quantitatively well the evolution of the Φ_{PL} with the Ag^+ content (Figure 4c). This indicates that, at room temperature, the main effect of Na^+ cations is to suppress nonradiative decay pathways competing with the radiative recombination of TEs on a similar time scale. Despite the beneficial shielding effect by the Na^+ cations, Φ_{PL} was below 5% also in lightly Ag-substituted NCs ($x = 0.05$), which indicated that nonradiative processes likely associated with electron trapping in Bi^{3+} sites and phonon-mediated decay were still dominant over radiative recombination of the TE.

In order to probe the radiative PL decay kinetics and thereby evaluate the effects of Ag^+ substitution on the oscillator strength of TEs, we performed time-resolved PL measurements at cryogenic temperatures. Cooling the NCs dramatically lengthened their PL dynamics that reached a plateau for $T <$ 120 K (Figure S7), indicating that thermally assisted nonradiative channels were largely suppressed. As shown in Figure 5a, the PL decay curves at $T = 77$ K were well described by stretched exponential functions similar to the room-temperature kinetics, although with significantly larger β-factors than at 300 K (Figure S8), indicating reduced thermal disorder. We notice that also at 77 K the β-factor was slightly lower for larger x-values, consistent with the higher structural disorder already highlighted by the room-temperature data. The corresponding PL lifetimes were up to 3 orders of magnitude slower than at room temperature, and the corresponding radiative decay rates increased monotonically with increasing x (Figure 5b), suggesting that the addition of Ag^+ cations gradually enhanced the oscillator strength of TE transition.

To support this hypothesis, we computed the oscillator strength for TE transitions at the DFT/PBE level as a function of the number of Ag^+ cations surrounding a central $BiCl_6$ octahedron (Figure 5c). This was done by gradually replacing Na^+ ions with Ag^+ ions around the chosen Bi^{3+} ion. The substitution of Na^+ ions around one octahedron centered on a Bi ion either with 2 Ag^+ or with 4 Ag^+ leads to two possible configurations, *cis* or *trans*. In a random distribution of Na^+ and Ag^+ ions, the *cis* configuration is more plausible and is thus reported in Figure 5c. The oscillator strengths associated to the *trans* configurations are reported in Figure S9 for completeness. Overall, we observe that the oscillator strength increases

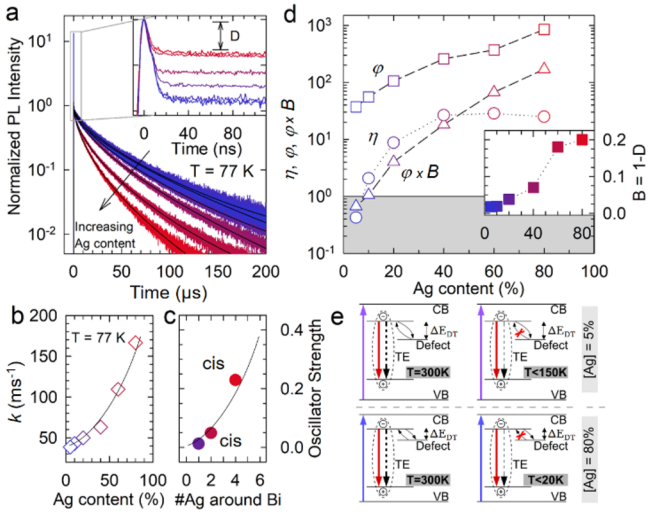

Figure 5. (a) Normalized PL decay traces of the $Cs_2Na_xAg_{1-x}InCl_6$ NCs at 77 K. The fitting curves to stretched exponential functions are shown as black lines. The respective β values are shown in Figure S8. Inset: Enlargement of the first 110 ns of the PL decay, highlighting the emergence of the fast decay portion that is directly proportional to the fraction of dark NCs, *D*. (b) Radiative recombination rate, *k*, of the PL decay traces reported in panel a as a function of the Ag^+ content. The black line is a guide for the eyes. (c) Oscillator strength of the TE recombination pathway (CBM → VBM transition) obtained by the DFT calculations as a function of the number of $AgCl_6$ octahedra surrounding a central $BiCl_6$ octahedron in a $Cs_2NaBiCl_6$ 2 × 2× 2 supercell. In the case of 2 and 4 Ag ions, the reported oscillator strengths are relative to the *cis* configurations (see the Supporting Information for further details). The black line is a guide for the eyes. (d) Static (η) and dynamic (φ) brightening factors and the product of $\varphi \times B$ as a function of x. The gray shading corresponds to *y*-axis <1. Inset: The term $B = 1 - D$ representing the fraction of emissive TEs as a function of x. (e) Schematics of the energy diagram of the $Cs_2Na_{0.95}Ag_{0.05}InCl_6$ (top) and $Cs_2Na_{0.2}Ag_{0.8}InCl_6$ NCs (bottom). The same color scheme applies to all panels. All measurements were conducted using an excitation energy of 3.5 eV and a pulse frequency of 140 Hz. The color scheme in all panels refers to the code reported in Figure 4a.

at increasing amount of Ag^+ ions comparing well with the monotonic increase of the radiative recombination rates observed experimentally (Figure 5b).

The low-temperature PL studies enabled us to gather deeper insights into the mechanism of carrier trapping that was found to correlate with the DFT-predicted role of Bi-related surface defects. Specifically, the lengthening of the PL dynamics suggested that the Φ_{PL} of all investigated systems was enhanced at cryogenic temperatures with respect to $T = 300$ K. This behavior is quantified by the *dynamic* brightening factor $\varphi = \tau^{77K}/\tau^{300K}$ reported in Figure 5d, which represents the relative increase of Φ_{PL} expected solely based on the lengthening of the PL decay traces at low T. Interestingly, while following a qualitatively similar trend with the Ag^+ content, φ systematically exceeded by at least 10 fold the respective relative PL enhancement measured in continuous-wave (cw) conditions, expressed through the *static* brightening factor, η (extracted as the ratio between the PL efficiency at 77 and 300 K measured using cw excitation, Figure S10). This indicated that, at low temperature, the emission yield of our NCs was less than 10% of the respective intrinsic value represented by φ, suggesting that the population of emitting

https://dx.doi.org/10.1021/acsenergylett.0c00914
ACS Energy Lett. 2020, 5, 1840−1847

NC had dropped with respect to room temperature. For x = 0.05, η showed the minimum value of ∼0.3, indicating that for such NCs, Φ_{PL} was *lower* at T = 77 K with respect to T = 300 K, despite the respective lifetime had significantly *lengthened* (Figures 5a).

This surprising behavior suggested that the photophysical mechanism responsible for the optical properties of $Cs_2Na_{1-x}Ag_xBiCl_6$ NCs was more complex than the mere competition between radiative recombination of TEs and their thermal-assisted nonradiative decay. This was revealed by the analysis of the initial fast component of the low-temperature PL decay curves shown in the inset of Figure 5a. At T = 77 K, all NCs showed a resolution-limited PL drop, whose relative intensity (indicated as D) with respect to the long-lived PL decay decreased with increasing x. In light of the DFT study suggesting the presence of electron-accepting sites associated to under-coordinated surface Bi atoms, we ascribe this decay to the rapid dissociation of TEs by nonradiative electron trapping, which rendered a fraction of our NCs nonemissive or dark. As a result of this process, with increasing Ag^+ content, the complementary fraction of emissive (or bright, B) NCs in the ensemble, expressed as $B = 1 - D$, monotonically grew, as shown in the inset of Figure 5d. Consistent with this picture, by scaling the dynamic brightening factor for the evolution of the bright NC population at low temperature through the product $\varphi \times B$, we reproduced the x-trend of η (Figure 5e), including the low-T drop of Φ_{PL} for x = 0.05.

Considering the whole body of spectroscopic data and DFT calculations, we model the effect of both temperature and Ag^+ substitution on the recombination of TEs according to the scheme depicted in Figure 5e. For any x-value, at 300 K, the radiative recombination of the TE competes mostly with phonon-assisted nonradiative recombination likely associated to a combination of vibrational quenching and electron trapping in Bi-related surface defects. The latter effect is, however, compensated by efficient thermal electron detrapping. At low temperatures, on the other hand, the emission efficiency is determined by the interplay between the beneficial suppression of such a temperature-assisted nonradiative decay channel for TEs and the detrimental effect of reduced thermal detrapping of electrons trapped in surface defects. At a given temperature, the latter effect depends strongly on the depths of the electron trap. Consistently, NCs with low Ag^+ content showed the largest trapping-related PL drop (hence lowest B-values), because in such NCs, electron traps associated to undercoordinated Bi atoms were deeper in the forbidden gap. One key consequence of this mechanism is that NCs with higher Ag^+ content (showing relatively larger B-values at T = 77 K) approach the behavior of lightly Ag-substituted NCs, featuring shallow electron traps, upon lowering the temperature further. This is highlighted by the evolution of the spectral and dynamic properties of NCs featuring x = 0.05 and x = 0.8 from 300 to 3.5 K reported in Figures S11−S14 and discussed in detail in Supplementary Discussion 1. Importantly, such side-by-side experiments corroborate the theoretical findings and show that the activation energy for electron detrapping drops from ΔE_{DT} = 102 meV for x = 0.05 to ΔE_{DT} = 2 meV for x = 0.8.

In summary, we have developed a hot injection synthesis approach to prepare $Cs_2NaBiCl_6$ NCs which we systematically alloyed with Ag^+ cations to form $Cs_2Na_{1-x}Ag_xBiCl_6$ NCs. While pure $Cs_2NaBiCl_6$ NCs did not exhibit any PL emission, the incorporation of Ag^+ cations, to form $Cs_2Na_{1-x}Ag_xBiCl_6$ NCs, led to the emergence of a broad PL band (fwhm ≈ 550 meV) peaked at around 1.8 eV and characterized by a large Stokes shift (ranging from ∼1.9 eV for x = 0.05 to ∼1.5 eV for x = 1). The PL efficiency of these NCs was maximized for low amounts of Ag^+ incorporated, reaching ∼3% for x = 0.05. These optical features were consistent with a trapped exciton emission mechanism. Indeed, our DFT calculations indicated that in a Na-rich (hence Ag-poor) $Cs_2Na_{1-x}Ag_xBiCl_6$ system, Ag^+ ions act as centers that are able to localize both holes and electrons at the band edges. On the other hand, the low Φ_{PL} for the whole batch of systems could be ascribed to the presence of nonradiative quenching mechanisms dominated by the presence of surface traps. In particular, undercoordinated Bi^{3+} ions, which are generated from an incomplete surface passivation after synthesis and/or washing, create an empty electronic trapping state below the conduction band, whose energy is modulated according to the Na/Ag ratio. The depth of such trap states was probed at various temperatures by measuring the PL emission efficiency, which confirmed that the trapping/detrapping rate increased with the concentrations of Ag. In practice, the system that shows the most efficient TE mechanism is also the one that has efficient concomitant nonradiative pathways, thus reducing the overall performance of the DP material. These results provide a gateway to design new materials to maximize their optoelectronic efficiency.

■ ASSOCIATED CONTENT

Supporting Information

The Supporting Information is available free of charge at https://pubs.acs.org/doi/10.1021/acsenergylett.0c00914.

XPS and SEM-EDS elemental analyses, TEM images and size distribution histograms of $Cs_2Na_{1-x}Ag_xBiCl_6$ NCs, electronic structure of $Cs_2Na_{1-x}Ag_xBiCl_6$ NC models, PLE curves, PL spectra at different temperatures, PL decay times, PL peak maximum, and fwhm of the PL peaks as a function of the temperature (PDF)

■ AUTHOR INFORMATION

Corresponding Authors

Ivan Infante − *Nanochemistry Department, Istituto Italiano di Tecnologia, 16163 Genova, Italy; Department of Theoretical Chemistry, Vrije Universiteit Amsterdam, 1081 HV Amsterdam, The Netherlands;* orcid.org/0000-0003-3467-9376; Email: ivan.infante@iit.it

Luca De Trizio − *Nanochemistry Department, Istituto Italiano di Tecnologia, 16163 Genova, Italy;* orcid.org/0000-0002-1514-6358; Email: luca.detrizio@iit.it

Liberato Manna − *Nanochemistry Department, Istituto Italiano di Tecnologia, 16163 Genova, Italy;* orcid.org/0000-0003-4386-7985; Email: liberato.manna@iit.it

Sergio Brovelli − *Dipartimento di Scienza dei Materiali, Universitá degli Studi di Milano-Bicocca, 20125 Milano, Italy;* orcid.org/0000-0002-5993-855X; Email: sergio.brovelli@unimib.it

Authors

Dongxu Zhu − *Department of Chemistry, School of Science, Beijing JiaoTong University, Beijing 100044, China; Nanochemistry Department, Istituto Italiano di Tecnologia, 16163 Genova, Italy*

https://dx.doi.org/10.1021/acsenergylett.0c00914
ACS Energy Lett. 2020, 5, 1840−1847

Juliette Zito − *Nanochemistry Department, Istituto Italiano di Tecnologia, 16163 Genova, Italy; Dipartimento di Chimica e Chimica Industriale, Università di Genova, 16146 Genova, Italy*
Valerio Pinchetti − *Dipartimento di Scienza dei Materiali, Universitá degli Studi di Milano-Bicocca, 20125 Milano, Italy;* orcid.org/0000-0003-3792-3661
Zhiya Dang − *Nanochemistry Department, Istituto Italiano di Tecnologia, 16163 Genova, Italy*
Andrea Olivati − *Dipartimento di Scienza dei Materiali, Universitá degli Studi di Milano-Bicocca, 20125 Milano, Italy*
Lea Pasquale − *Materials Characterization Facility, Istituto Italiano di Tecnologia, 16163 Genova, Italy*
Aiwei Tang − *Department of Chemistry, School of Science, Beijing JiaoTong University, Beijing 100044, China;* orcid.org/0000-0002-0716-0387
Matteo L. Zaffalon − *Dipartimento di Scienza dei Materiali, Universitá degli Studi di Milano-Bicocca, 20125 Milano, Italy*
Francesco Meinardi − *Dipartimento di Scienza dei Materiali, Universitá degli Studi di Milano-Bicocca, 20125 Milano, Italy*

Complete contact information is available at: https://pubs.acs.org/10.1021/acsenergylett.0c00914

Author Contributions

[▽]D.Z., J.Z., and V.P. contributed equally to this work.

Notes

The authors declare no competing financial interest.

■ ACKNOWLEDGMENTS

We thank Simone Lauciello for carrying out the SEM-EDS measurements. D.Z. acknowledges a scholarship from the China Scholarship Council (CSC) (201807090085). I.I. acknowledges The Netherlands Organization of Scientific Research (NWO) through the Innovational Research Incentive (Vidi) Scheme (Grant No. 723.013.002). The computational work was carried out on the Dutch national e-infrastructure with the support of the SURF Co-operative. Financial support from the Italian Ministry of University and Research (MIUR) through grant "Dipartimenti di Eccellenza-2017 Materials For Energy" is gratefully acknowledge. We also acknowledge funding from the programme for research and Innovation Horizon 2020 (2014−2020) under the Marie Skłodowska-Curie Grant Agreement COMPASS No. 691185.

■ REFERENCES

(1) D'Innocenzo, V.; Srimath Kandada, A. R.; De Bastiani, M.; Gandini, M.; Petrozza, A. Tuning the Light Emission Properties by Band Gap Engineering in Hybrid Lead Halide Perovskite. *J. Am. Chem. Soc.* **2014**, *136* (51), 17730−17733.
(2) Stranks, S. D.; Snaith, H. J. Metal-halide perovskites for photovoltaic and light-emitting devices. *Nat. Nanotechnol.* **2015**, *10*, 391.
(3) Luo, X.; Ding, T.; Liu, X.; Liu, Y.; Wu, K. Quantum-Cutting Luminescent Solar Concentrators Using Ytterbium-Doped Perovskite Nanocrystals. *Nano Lett.* **2019**, *19* (1), 338−341.
(4) Akkerman, Q. A.; Rainò, G.; Kovalenko, M. V.; Manna, L. Genesis, challenges and opportunities for colloidal lead halide perovskite nanocrystals. *Nat. Mater.* **2018**, *17* (5), 394−405.
(5) Meinardi, F.; Akkerman, Q. A.; Bruni, F.; Park, S.; Mauri, M.; Dang, Z.; Manna, L.; Brovelli, S. Doped Halide Perovskite Nanocrystals for Reabsorption-Free Luminescent Solar Concentrators. *ACS Energy Letters* **2017**, *2* (10), 2368−2377.
(6) Shamsi, J.; Urban, A. S.; Imran, M.; De Trizio, L.; Manna, L. Metal Halide Perovskite Nanocrystals: Synthesis, Post-Synthesis Modifications, and Their Optical Properties. *Chem. Rev.* **2019**, *119* (5), 3296−3348.
(7) Snaith, H. J. Present status and future prospects of perovskite photovoltaics. *Nat. Mater.* **2018**, *17* (5), 372−376.
(8) Fu, H. Review of lead-free halide perovskites as light-absorbers for photovoltaic applications: From materials to solar cells. *Sol. Energy Mater. Sol. Cells* **2019**, *193*, 107−132.
(9) Ghosh, S.; Pradhan, B. Lead-Free Metal Halide Perovskite Nanocrystals: Challenges, Applications, and Future Aspects. *ChemNanoMat* **2019**, *5* (3), 300−312.
(10) Giustino, F.; Snaith, H. J. Toward Lead-Free Perovskite Solar Cells. *ACS Energy Letters* **2016**, *1* (6), 1233−1240.
(11) Igbari, F.; Wang, Z.-K.; Liao, L.-S. Progress of Lead-Free Halide Double Perovskites. *Adv. Energy Mater.* **2019**, *9* (12), 1803150.
(12) Zhang, Z.; Wu, C.; Wang, D.; Liu, G.; Zhang, Q.; Luo, W.; Qi, X.; Guo, X.; Zhang, Y.; Lao, Y.; Qu, B.; Xiao, L.; Chen, Z. Improvement of $Cs_2AgBiBr_6$ double perovskite solar cell by rubidium doping. *Org. Electron.* **2019**, *74*, 204−210.
(13) Kung, P.-K.; Li, M.-H.; Lin, P.-Y.; Jhang, J.-Y.; Pantaler, M.; Lupascu, D. C.; Grancini, G.; Chen, P. Lead-Free Double Perovskites for Perovskite Solar Cells. *Solar RRL* **2020**, *4* (2), 1900306.
(14) Wu, C.; Zhang, Q.; Liu, Y.; Luo, W.; Guo, X.; Huang, Z.; Ting, H.; Sun, W.; Zhong, X.; Wei, S.; Wang, S.; Chen, Z.; Xiao, L. The Dawn of Lead-Free Perovskite Solar Cell: Highly Stable Double Perovskite $Cs_2AgBiBr_6$ Film. *Advanced Science* **2018**, *5* (3), 1700759.
(15) Luo, J.; Wang, X.; Li, S.; Liu, J.; Guo, Y.; Niu, G.; Yao, L.; Fu, Y.; Gao, L.; Dong, Q.; Zhao, C.; Leng, M.; Ma, F.; Liang, W.; Wang, L.; Jin, S.; Han, J.; Zhang, L.; Etheridge, J.; Wang, J.; Yan, Y.; Sargent, E. H.; Tang, J. Efficient and stable emission of warm-white light from lead-free halide double perovskites. *Nature* **2018**, *563* (7732), 541−545.
(16) Locardi, F.; Sartori, E.; Buha, J.; Zito, J.; Prato, M.; Pinchetti, V.; Zaffalon, M. L.; Ferretti, M.; Brovelli, S.; Infante, I.; De Trizio, L.; Manna, L. Emissive Bi-Doped Double Perovskite $Cs_2Ag_{1-x}Na_xInCl_6$ Nanocrystals. *ACS Energy Letters* **2019**, *4*, 1976−1982.
(17) Chen, N.; Cai, T.; Li, W.; Hills-Kimball, K.; Yang, H.; Que, M.; Nagaoka, Y.; Liu, Z.; Yang, D.; Dong, A.; Xu, C.-Y.; Zia, R.; Chen, O. Yb- and Mn-Doped Lead-Free Double Perovskite Cs_2AgBiX_6 (X = Cl^-, Br^-) Nanocrystals. *ACS Appl. Mater. Interfaces* **2019**, *11* (18), 16855−16863.
(18) Locardi, F.; Cirignano, M.; Baranov, D.; Dang, Z.; Prato, M.; Drago, F.; Ferretti, M.; Pinchetti, V.; Fanciulli, M.; Brovelli, S.; De Trizio, L.; Manna, L. Colloidal Synthesis of Double Perovskite $Cs_2AgInCl_6$ and Mn-Doped $Cs_2AgInCl_6$ Nanocrystals. *J. Am. Chem. Soc.* **2018**, *140* (40), 12989−12995.
(19) Lee, W.; Hong, S.; Kim, S. Colloidal Synthesis of Lead-Free Silver-Indium Double-Perovskite $Cs_2AgInCl_6$ Nanocrystals and Their Doping with Lanthanide Ions. *J. Phys. Chem. C* **2019**, *123* (4), 2665−2672.
(20) Dahl, J. C.; Osowiecki, W. T.; Cai, Y.; Swabeck, J. K.; Bekenstein, Y.; Asta, M.; Chan, E. M.; Alivisatos, A. P. Probing the Stability and Band Gaps of $Cs_2AgInCl_6$ and $Cs_2AgSbCl_6$ Lead-Free Double Perovskite Nanocrystals. *Chem. Mater.* **2019**, *31* (9), 3134−3143.
(21) Yang, B.; Hong, F.; Chen, J.; Tang, Y.; Yang, L.; Sang, Y.; Xia, X.; Guo, J.; He, H.; Yang, S.; Deng, W.; Han, K. Colloidal Synthesis and Charge-Carrier Dynamics of $Cs_2AgSb_{1-y}Bi_yX_6$ (X: Br, Cl; $0 \le y \le 1$) Double Perovskite Nanocrystals. *Angew. Chem., Int. Ed.* **2019**, *58* (8), 2278−2283.
(22) Khalfin, S.; Bekenstein, Y. Advances in lead-free double perovskite nanocrystals, engineering band-gaps and enhancing stability through composition tunability. *Nanoscale* **2019**, *11* (18), 8665−8679.
(23) Liu, Y.; Jing, Y.; Zhao, J.; Liu, Q.; Xia, Z. Design Optimization of Lead-Free Perovskite $Cs_2AgInCl_6$:Bi Nanocrystals with 11.4% Photoluminescence Quantum Yield. *Chem. Mater.* **2019**, *31* (9), 3333−3339.
(24) Creutz, S. E.; Crites, E. N.; De Siena, M. C.; Gamelin, D. R. Colloidal Nanocrystals of Lead-Free Double-Perovskite (Elpasolite)

Semiconductors: Synthesis and Anion Exchange To Access New Materials. *Nano Lett.* **2018**, *18* (2), 1118−1123.
(25) Bekenstein, Y.; Dahl, J. C.; Huang, J.; Osowiecki, W. T.; Swabeck, J. K.; Chan, E. M.; Yang, P.; Alivisatos, A. P. The Making and Breaking of Lead-Free Double Perovskite Nanocrystals of Cesium Silver-Bismuth Halide Compositions. *Nano Lett.* **2018**, *18* (6), 3502−3508.
(26) Du, K.-z.; Meng, W.; Wang, X.; Yan, Y.; Mitzi, D. B. Bandgap Engineering of Lead-Free Double Perovskite $Cs_2AgBiBr_6$ through Trivalent Metal Alloying. *Angew. Chem., Int. Ed.* **2017**, *56* (28), 8158−8162.
(27) Karmakar, A.; Dodd, M. S.; Agnihotri, S.; Ravera, E.; Michaelis, V. K. Cu(II)-Doped $Cs_2SbAgCl_6$ Double Perovskite: A Lead-Free, Low-Bandgap Material. *Chem. Mater.* **2018**, *30* (22), 8280−8290.
(28) Majher, J. D.; Gray, M. B.; Strom, T. A.; Woodward, P. M. $Cs_2NaBiCl_6$:Mn^{2+} - A New Orange-Red Halide Double Perovskite Phosphor. *Chem. Mater.* **2019**, *31* (5), 1738−1744.
(29) Yang, B.; Mao, X.; Hong, F.; Meng, W.; Tang, Y.; Xia, X.; Yang, S.; Deng, W.; Han, K. Lead-Free Direct Band Gap Double-Perovskite Nanocrystals with Bright Dual-Color Emission. *J. Am. Chem. Soc.* **2018**, *140* (49), 17001−17006.
(30) Lamba, R. S.; Basera, P.; Bhattacharya, S.; Sapra, S. Band Gap Engineering in $Cs_2(Na_xAg_{1-x})BiCl_6$ Double Perovskite Nanocrystals. *J. Phys. Chem. Lett.* **2019**, *10*, 5173−5181.
(31) Tran, T. T.; Panella, J. R.; Chamorro, J. R.; Morey, J. R.; McQueen, T. M. Designing indirect-direct bandgap transitions in double perovskites. *Mater. Horiz.* **2017**, *4* (4), 688−693.
(32) Meng, W.; Wang, X.; Xiao, Z.; Wang, J.; Mitzi, D. B.; Yan, Y. Parity-Forbidden Transitions and Their Impact on the Optical Absorption Properties of Lead-Free Metal Halide Perovskites and Double Perovskites. *J. Phys. Chem. Lett.* **2017**, *8* (13), 2999−3007.
(33) Meinardi, F.; Bruni, F.; Brovelli, S. Luminescent solar concentrators for building-integrated photovoltaics. *Nature Reviews Materials* **2017**, *2*, 17072.
(34) Mahor, Y.; Mir, W. J.; Nag, A. Synthesis and Near-Infrared Emission of Yb-Doped $Cs_2AgInCl_6$ Double Perovskite Microcrystals and Nanocrystals. *J. Phys. Chem. C* **2019**, *123* (25), 15787−15793.
(35) Bodnarchuk, M. I.; Boehme, S. C.; ten Brinck, S.; Bernasconi, C.; Shynkarenko, Y.; Krieg, F.; Widmer, R.; Aeschlimann, B.; Günther, D.; Kovalenko, M. V.; Infante, I. Rationalizing and Controlling the Surface Structure and Electronic Passivation of Cesium Lead Halide Nanocrystals. *ACS Energy Letters* **2019**, *4* (1), 63−74.
(36) Kshirsagar, A. S.; Nag, A. Synthesis and optical properties of colloidal $Cs_2AgSb_{1-x}Bi_xCl_6$ double perovskite nanocrystals. *J. Chem. Phys.* **2019**, *151* (16), 161101.
(37) Manna, D.; Das, T. K.; Yella, A. Tunable and Stable White Light Emission in Bi^{3+}-Alloyed $Cs_2AgInCl_6$ Double Perovskite Nanocrystals. *Chem. Mater.* **2019**, *31* (24), 10063−10070.
(38) Gray, M. B.; Majher, J. D.; Strom, T. A.; Woodward, P. M. Broadband White Emission in $Cs_2AgIn_{1-x}Bi_xCl_6$ Phosphors. *Inorg. Chem.* **2019**, *58* (19), 13403−13410.
(39) Giansante, C.; Infante, I. Surface Traps in Colloidal Quantum Dots: A Combined Experimental and Theoretical Perspective. *J. Phys. Chem. Lett.* **2017**, *8* (20), 5209−5215.
(40) Houtepen, A. J.; Hens, Z.; Owen, J. S.; Infante, I. On the Origin of Surface Traps in Colloidal II-VI Semiconductor Nanocrystals. *Chem. Mater.* **2017**, *29* (2), 752−761.
(41) ten Brinck, S.; Zaccaria, F.; Infante, I. Defects in Lead Halide Perovskite Nanocrystals: Analogies and (Many) Differences with the Bulk. *ACS Energy Letters* **2019**, *4* (11), 2739−2747.

https://dx.doi.org/10.1021/acsenergylett.0c00914
ACS Energy Lett. 2020, 5, 1840−1847